3. Predictions obtained using a solid diffusion analysis ⸻ ⸻ ⸻ ⸺g from the grain boundaries toward the grain centers and local equilibriu⸺ ⸺ng interface are consistent with the measured temperature vs. time curves. Spe⸺cally, initial melting at the solidus involves only a small volume of material due to the limited solid diffusion. Moreover, the majority of the enthalpy input is absorbed near the liquidus temperature, causing the formation of the plateau near this temperature. The analysis accurately describes the observed effect of heating rate and grain size variations.

4. The highest melting speed obtained in these experiments, i.e. for the largest grain size and fastest heating rate, is only ~0.2 cm/s, a speed apparently not rapid enough to cause a loss of local equilibrium at the melt interface in this alloy system.

5. This interpretation of the temperature vs. time curves enables a method to measure liquidus and solidus temperatures of refractory alloys.

Acknowledgment

References

1. Cezairliyan, A., Int. *J. Thermophys.*, 5 (1984), 177-193.
2. Cezairliyan, A., *High Temp. Sci.*, 4 (1972), 248-252.
3. Verhoeven, J.D., and Gibson, E.D., *Metall. Trans.*, 2 (1971), 3021-3026.
4. Wan, X., Han, Q., and Hunt, J.D., *Met. & Mat. Trans.*, 29A (1998), 751-755.
5. Kumar, K.C.H., Wollants, P., and Delaey, L., *Calphad*, 18 (1994), 71-79.
6. D. Basak, W.J. Boettinger, D. Josell, S. R. Coriell, J. McClure, S. Krishnan and A. Cezairliyan, *Acta Mater.*, 47 (1999), 3147-3158.
7. Cezairliyan, A., Krishnan, S., and McClure, J.L., *Int. J. Thermophys.*, 17 (1996), 1455-1473.
8. Kaschnitz, E., and Cezairliyan, A., *Int. J. Thermophys.*, 17 (1996), 1069-1078.
9. Cezairliyan, A., Foley, G.M., Morse, M.S., and Miiller, A.P., *in Temperature - Its Measurement and Control in Science and Industry*, vol. 6, ed. J.F. Schooley (AIP, New York, 1992), 757-762.
10. Cezairliyan, A., Morse, M. S., Berman, H.A., and Beckett, C.W., *J. Res. Natl. Bur. Stand. (U.S.)*, 74A (1970), 65-92.
11 Cezairliyan, A., *J. Res. Natl. Bur. Stand. (U.S.)*, 75C (1971), 7-18.
12. T. Matsumoto and A. Cezairliyan, *Int. J. Thermophys.*, 18 (1997), 1539-1556.
13. Preston-Thomas, H., *Metrologia*, 27 (1990), 3-10 and 107.
14. Cezairliyan, A., and Miiller, A., Int. *J. Thermophys.*, 13 (1992), 39-55.
15. Verhoeven, J.D., and Gibson, E.D., *J. Crystal Growth*, 11 (1971), 39-49.
16. Allen, W.P., Fecht, H.J., and Perepezko, *J.H., Scripta Met.*, 23 (1989), 643-648.
17. Baker, J.C.,and Cahn, J.W., in *Solidification* (ASM, Metals Park, OH, 1971), 23-58.
18. Smithells, C. J., *Metals Reference Book*, 4th edition, (Butterworths, London, 1967), 659.
19. Rettenmayr, M., Warkentin O., and Exner, H.E., *Zeit. fuer Metallkunde*, 88 (1997), 617-619.
20. Rettenmayr, M., Warkentin O., Rappaz M., Exner, H.E., *Acta Materialia*, 49 (2001), 2499-2510.
21. Aziz, M.J., and Boettinger, W.J., *Acta Metall. Mater.,* 42 (1994), 527-537.
22. Aziz, M.J., *Met. Trans.,* 27A (1996), 671-686.
23. Ahmad, A., Wheeler, A.A., Boettinger, W.J., and McFaddden, G.B., *Phys. Rev. E*, 58 (1998), 3436-3450.

ON THE INTERACTION BETWEEN MACROSEGREGATION, SHRINKAGE FLOW AND GRAIN MOVEMENT

Andreas Ludwig and Menghuai Wu

University of Leoben, Department of Metallurgy
Frank-Josef-Strasse 18
A – 8700 Leoben, Austria

Abstract

A two-phase volume averaging model was used to study convection and grain movement, and their influence on the formation of macrosegregations. In the model both liquid and solid phases were treated as separate interpenetrating continua. The mass, momentum, species and enthalpy conservation equations for each phase and a grain transport equation were coupled. An ingot casting (Al-4 wt.% Cu) with near globular solidification morphology was simulated. Different formation mechanisms for negative and positive segregated regions are discussed. The importance of grain movement for the formation of macrosegregations is demonstrated by comparing two distinct cases: one with grain movement and shrinkage flow and the second with only shrinkage flow.

Introduction

Melt convection and grain movement play an important role in solidification of castings. Different macrosegregation patterns are formed, or at least strongly influenced, by melt flow and grain movement[1-3]. Numerical methods to study these phenomena have only been developed in recent years, when the conservation equations of mass, momentum, energy, and solute could be coupled and solved simultaneously.

The most often used numerical approach is based on a 'mixture' theory[4-11] which treats the two-phase problem (liquid and solid) as a single, pseudo-fluid, phase. The transport equations, which were supposed to be equally valid in bulk melt, mushy zone and solid regions by assigning respective 'physical properties', were solved with a single-domain numerical method on a fixed grid. The obvious drawback of this 'mixture' model is that it fails to describe the interaction between the liquid and solid phases, and the thermal and constitutional non-equilibrium at the liquid-solid interface. An other numerical approach is a multiphase model based on volume averaging such as the one developed by Beckermann's group[12-18]. They treated the liquid and solid as separate interpenetrating continua and established and solved the transport equations for mass, momentum, energy and solute simultaneously for both the liquid and solid. Thereby they carried out a rigorous description of disparate solid and liquid velocities, interactions, thermal and constitutional non-equilibrium, and many other microscopic phenomena. With the two-phase volume averaging approach used in this paper the authors[19-24] focus on globular equiaxed solidification, and therefore some parameters used in the Beckermann's model[7-8,12] to describe the dendritic solidification morphology were avoided. Together with[25] we believe that further studies are necessary to understand and describe the dendritic morphology.

In this paper the two-phase globular equiaxed solidification model was used to study the interaction between macrosegregation, shrinkage flow and grain movement. Both the nucleation law and the growth kinetics[26-28] were implemented in the macro transport equations. An Al-4 wt.% Cu ingot casting was simulated. With a ppm of Ti as the grain refiner this alloy solidifies with a near globular equiaxed rather than a distinct dendritic morphology. Emphases were placed on flow induced by solidification shrinkage and grain movement, and their influence on and the formation of macrosegregation.

Modeling and Numerical Procedure

The two-phase volume averaging model for globular equiaxed solidification[19-24] was described previously, and therefore, only a short description is presented here. The conservation equations, source terms, exchange terms and some auxiliary terms are listed in Table I. Derivation of the equations and description of the volume averaging theorem are detailed in the literature[12,19].

Conservation Equations

The liquid and solid phases are transported according to the mass and momentum conservation, Eqs. (1)+(2) taking solidification (or remelting) into account by a mass transfer term $M_{ls}(=-M_{sl})$ defined in Eq. (7). Details of M_{ls} are given below. The volume fractions of both phases is subject to $f_l + f_s = 1$.

A 'viscosity' of the solid, μ_s, in the momentum conservation Eq. (2) is employed. It is empirically defined in Eq. (13) based on the mixing rule:[13, 14-16] $\mu_{mix} = f_l\mu_l + f_s\mu_s$. μ_s is in the same order than μ_l for small f_s. As the f_s approaches the packing limit f_s^c, which is taken as 0.637 for globular grains, μ_s increases to infinitely. Therefore, beyond the packing limit the solid becomes rigid. However, the melt may penetrate the voids of the closely packed grains (see below).

Momentum exchange $\vec{U}_{ls}(=-\vec{U}_{sl})$ consists of two parts: one due to mass transfer $\vec{U}_{ls}^p$ and the other due to friction and drag $\vec{U}_{ls}^d$. Both terms are given in Eq. (8). In order to define $\vec{U}_{ls}^p$, two different situations must be considered: solidification and remelting. For solidification, the momentum transferred from liquid to solid is determined by the velocity of the melt $\vec{u}_l$ and the mass transfer rate M_{ls}, hence $\vec{U}_{ls}^p = \vec{u}^* \cdot M_{ls}$ with $\vec{u}^* = \vec{u}_l$. By analogy we have $\vec{U}_{ls}^p = \vec{u}^* \cdot M_{ls}$ with $\vec{u}^* = \vec{u}_s$ for remelting. In the friction and drag term $\vec{U}_{ls}^d$, there are two situations: below and beyond the packing limit f_s^c. For the low fraction solid ($f_s < f_s^c$), the solidified grains behave analogously to submerging objects, and therefore we used the Kozeny-Karman[26] model. Beyond the packing limit ($f_s \geq f_s^c$), we employed the porous medium model by Blake-Kozeny[29]. Details about these models are given elsewhere[19, 29-30].

The average solute concentrations in the melt, c_l, and in the solid, c_s, are obtained from the species conservation Eq. (3). The solute exchange $C_{ls}(=-C_{sl})$ between solid and liquid includes two parts: solute partitioning at the liquid-solid interface due to phase change C_{ls}^p and

Table I. Conservation equations, source and exchange terms and auxiliary equations for the numerical model of globular equiaxed solidification

	Conservation equations:	
Mass:	$\frac{\partial}{\partial t}(f_l\rho_l) + \nabla \cdot (f_l\rho_l\vec{u}_l) = M_{sl}$ $\frac{\partial}{\partial t}(f_s\rho_s) + \nabla \cdot (f_s\rho_s\vec{u}_s) = M_{ls}$	(1)
Momentum:	$\frac{\partial}{\partial t}(f_l\rho_l\vec{u}_l) + \nabla \cdot (f_l\rho_l\vec{u}_l \otimes \vec{u}_l) = -f_l\nabla p + \nabla \cdot \bar{\bar{\tau}}_l + f_l\rho_l\vec{g} + \vec{U}_{sl}$ $\frac{\partial}{\partial t}(f_s\rho_s\vec{u}_s) + \nabla \cdot (f_s\rho_s\vec{u}_s \otimes \vec{u}_s) = -f_s\nabla p + \nabla \cdot \bar{\bar{\tau}}_s + f_s\rho_s\vec{g} + \vec{U}_{ls}$ where $\bar{\bar{\tau}}_l = \mu_l f_l(\nabla \cdot \vec{u}_l + (\nabla \cdot \vec{u}_l)^T)$ and $\bar{\bar{\tau}}_s = \mu_s f_s(\nabla \cdot \vec{u}_s + (\nabla \cdot \vec{u}_s)^T)$	(2)
Species:	$\frac{\partial}{\partial t}(f_l\rho_l c_l) + \nabla \cdot (f_l\rho_l\vec{u}_l c_l) = \nabla \cdot (f_l\rho_l D_l \nabla c_l) + C_{sl}$ $\frac{\partial}{\partial t}(f_s\rho_s c_s) + \nabla \cdot (f_s\rho_s\vec{u}_s c_s) = \nabla \cdot (f_s\rho_s D_s \nabla c_s) + C_{ls}$	(3)
Enthalpy:	$\frac{\partial}{\partial t}(f_l\rho_l h_l) + \nabla \cdot (f_l\rho_l\vec{u}_l h_l) = \nabla \cdot (f_l k_l \nabla T_l) + Q_{sl}$ $\frac{\partial}{\partial t}(f_s\rho_s h_s) + \nabla \cdot (f_s\rho_s\vec{u}_s h_s) = \nabla \cdot (f_l k_s \nabla T_s) + Q_{ls}$ where $h_l = \int_{T_{ref}}^{T_l} c_{p(l)} dT + h_l^{ref}$ and $h_s = \int_{T_{ref}}^{T_s} c_{p(s)} dT + h_s^{ref}$	(4)
Grain transport:	$\frac{\partial}{\partial t} n + \nabla \cdot (\vec{u}_s n) = N$	(5)
	Source terms:	
Nucleation:	$N = \frac{d\Delta T}{dt} \cdot \frac{n_{max}}{\sqrt{2\pi} \cdot \Delta T_\sigma} \cdot e^{-\frac{1}{2}\left(\frac{\Delta T - \Delta T_N}{\Delta T_\sigma}\right)^2}$	(6)
	Exchange terms:	
Mass transfer	$M_{ls} = g_a \cdot \Delta c \cdot (n \cdot \pi d_s^2) \cdot \rho_s \cdot f_l$	(7)
Momentum:	$\vec{U}_{ls} = \vec{U}_{ls}^d + \vec{U}_{ls}^p$ $\qquad \vec{U}_{ls}^p = \vec{u}^* \cdot M_{ls}$ $\qquad \vec{U}_{ls}^d = K_{ls}(\vec{u}_l - \vec{u}_s)$	(8)
Species:	$C_{ls} = C_{ls}^d + C_{ls}^p$ $\qquad C_{ls}^p = c^* \cdot M_{ls}$ $\qquad C_{ls}^d$ neglected	(9)
Enthalpy:	$Q_{ls} = Q_{ls}^d + Q_{ls}^p$ $\qquad Q_{ls}^p = h^* \cdot M_{ls}$ $\qquad Q_{ls}^d = H^* \cdot (T_l - T_s)$	(10)
	Auxiliary terms:	
Mixture concentration:	$c_{mix} = \frac{c_l \cdot \rho_l \cdot f_l + c_s \cdot \rho_s \cdot f_s}{\rho_l \cdot f_l + \rho_s \cdot f_s}$	(11)
Grain diameter:	$d_s = \left(\frac{6 \cdot f_s}{\pi \cdot n}\right)^{\frac{1}{3}}$	(12)
Solid viscosity	$\mu_s = \begin{cases} \frac{\mu_l}{f_s} \cdot \left((1 - f_s/f_s^c)^{-2.5 f_s^c} - (1 - f_s)\right) & \text{when } f_s < f_s^c \\ \infty & \text{else} \end{cases}$	(13)

In this paper the two-phase globular equiaxed solidification model was used to study the interaction between macrosegregation, shrinkage flow and grain movement. Both the nucleation law and the growth kinetics[26-28] were implemented in the macro transport equations. An Al-4 wt.% Cu ingot casting was simulated. With a ppm of Ti as the grain refiner this alloy solidifies with a near globular equiaxed rather than a distinct dendritic morphology. Emphases were placed on flow induced by solidification shrinkage and grain movement, and their influence on and the formation of macrosegregation.

Modeling and Numerical Procedure

The two-phase volume averaging model for globular equiaxed solidification[19-24] was described previously, and therefore, only a short description is presented here. The conservation equations, source terms, exchange terms and some auxiliary terms are listed in Table I. Derivation of the equations and description of the volume averaging theorem are detailed in the literature[12,19].

Conservation Equations

The liquid and solid phases are transported according to the mass and momentum conservation, Eqs. (1)+(2) taking solidification (or remelting) into account by a mass transfer term $M_{ls}(=-M_{sl})$ defined in Eq. (7). Details of M_{ls} are given below. The volume fractions of both phases is subject to $f_l + f_s = 1$.

A 'viscosity' of the solid, μ_s, in the momentum conservation Eq. (2) is employed. It is empirically defined in Eq. (13) based on the mixing rule:[13, 14-16] $\mu_{mix} = f_l\mu_l + f_s\mu_l$. μ_s is in the same order than μ_l for small f_s. As the f_s approaches the packing limit f_s^c, which is taken as 0.637 for globular grains, μ_s increases to infinitely. Therefore, beyond the packing limit the solid becomes rigid. However, the melt may penetrate the voids of the closely packed grains (see below).

Momentum exchange $\vec{U}_{ls}(=-\vec{U}_{sl})$ consists of two parts: one due to mass transfer $\vec{U}_{ls}^p$ and the other due to friction and drag $\vec{U}_{ls}^d$. Both terms are given in Eq. (8). In order to define $\vec{U}_{ls}^p$, two different situations must be considered: solidification and remelting. For solidification, the momentum transferred from liquid to solid is determined by the velocity of the melt $\bar{u}_l$ and the mass transfer rate M_{ls}, hence $\vec{U}_{ls}^p = \bar{u}^* \cdot M_{ls}$ with $\bar{u}^* = \bar{u}_l$. By analogy we have $\vec{U}_{ls}^p = \bar{u}^* \cdot M_{ls}$ with $\bar{u}^* = \bar{u}_s$ for remelting. In the friction and drag term $\vec{U}_{ls}^d$, there are two situations: below and beyond the packing limit f_s^c. For the low fraction solid ($f_s < f_s^c$), the solidified grains behave analogously to submerging objects, and therefore we used the Kozeny-Karman[26] model. Beyond the packing limit ($f_s \geq f_s^c$), we employed the porous medium model by Blake-Kozeny[29]. Details about these models are given elsewhere[19, 29-30].

The average solute concentrations in the melt, c_l, and in the solid, c_s, are obtained from the species conservation Eq. (3). The solute exchange $C_{ls}(=-C_{sl})$ between solid and liquid includes two parts: solute partitioning at the liquid-solid interface due to phase change C_{ls}^p and

Table I. Conservation equations, source and exchange terms and auxiliary equations for the numerical model of globular equiaxed solidification

	Conservation equations:	
Mass:	$\frac{\partial}{\partial t}(f_l\rho_l) + \nabla \cdot (f_l\rho_l\bar{u}_l) = M_{sl}$ $\frac{\partial}{\partial t}(f_s\rho_s) + \nabla \cdot (f_s\rho_s\bar{u}_s) = M_{ls}$	(1)
Momentum:	$\frac{\partial}{\partial t}(f_l\rho_l\bar{u}_l) + \nabla \cdot (f_l\rho_l\bar{u}_l \otimes \bar{u}_l) = -f_l\nabla p + \nabla \cdot \bar{\bar{\tau}}_l + f_l\rho_l\bar{g} + \vec{U}_{sl}$ $\frac{\partial}{\partial t}(f_s\rho_s\bar{u}_s) + \nabla \cdot (f_s\rho_s\bar{u}_s \otimes \bar{u}_s) = -f_s\nabla p + \nabla \cdot \bar{\bar{\tau}}_s + f_s\rho_s\bar{g} + \vec{U}_{ls}$ where $\bar{\bar{\tau}}_l = \mu_l f_l(\nabla \cdot \bar{u}_l + (\nabla \cdot \bar{u}_l)^T)$ and $\bar{\bar{\tau}}_s = \mu_s f_s(\nabla \cdot \bar{u}_s + (\nabla \cdot \bar{u}_s)^T)$	(2)
Species:	$\frac{\partial}{\partial t}(f_l\rho_l c_l) + \nabla \cdot (f_l\rho_l\bar{u}_l c_l) = \nabla \cdot (f_l\rho_l D_l \nabla c_l) + C_{sl}$ $\frac{\partial}{\partial t}(f_s\rho_s c_s) + \nabla \cdot (f_s\rho_s\bar{u}_s c_s) = \nabla \cdot (f_s\rho_s D_s \nabla c_s) + C_{ls}$	(3)
Enthalpy:	$\frac{\partial}{\partial t}(f_l\rho_l h_l) + \nabla \cdot (f_l\rho_l\bar{u}_l h_l) = \nabla \cdot (f_l k_l \nabla T_l) + Q_{sl}$ $\frac{\partial}{\partial t}(f_s\rho_s h_s) + \nabla \cdot (f_s\rho_s\bar{u}_s h_s) = \nabla \cdot (f_l k_s \nabla T_s) + Q_{ls}$ where $h_l = \int_{T_{ref}}^{T_l} c_{p(l)} dT + h_l^{ref}$ and $h_s = \int_{T_{ref}}^{T_s} c_{p(s)} dT + h_s^{ref}$	(4)
Grain transport:	$\frac{\partial}{\partial t} n + \nabla \cdot (\bar{u}_s n) = N$	(5)
	Source terms:	
Nucleation:	$N = \frac{d\Delta T}{dt} \cdot \frac{n_{max}}{\sqrt{2\pi} \cdot \Delta T_\sigma} \cdot e^{-\frac{1}{2}\left(\frac{\Delta T - \Delta T_n}{\Delta T_\sigma}\right)^2}$	(6)
	Exchange terms:	
Mass transfer	$M_{ls} = g_\alpha \cdot \Delta c \cdot (n \cdot \pi d_s^2) \cdot \rho_s \cdot f_l$		(7)
Momentum:	$\vec{U}_{ls} = \vec{U}_{ls}^d + \vec{U}_{ls}^p$	$\vec{U}_{ls}^p = \bar{u}^* \cdot M_{ls}$	$\vec{U}_{ls}^d = K_{ls}(\bar{u}_l - \bar{u}_s)$	(8)
Species:	$C_{ls} = C_{ls}^d + C_{ls}^p$	$C_{ls}^p = c^* \cdot M_{ls}$	C_{ls}^d neglected	(9)
Enthalpy:	$Q_{ls} = Q_{ls}^d + Q_{ls}^p$	$Q_{ls}^p = h^* \cdot M_{ls}$	$Q_{ls}^d = H^* \cdot (T_l - T_s)$	(10)
	Auxiliary terms:	
Mixture concentration:	$c_{mix} = \frac{c_l \cdot \rho_l \cdot f_l + c_s \cdot \rho_s \cdot f_s}{\rho_l \cdot f_l + \rho_s \cdot f_s}$	(11)
Grain diameter:	$d_s = \left(\frac{6 \cdot f_s}{\pi \cdot n}\right)^{\frac{1}{3}}$	(12)
Solid viscosity	$\mu_s = \begin{cases} \frac{\mu_l}{f_s} \cdot \left((1 - f_s/f_s^c)^{-2.5 f_s^c} - (1 - f_s)\right) & \text{when } f_s < f_s^c \\ \infty & \text{else} \end{cases}$	(13)

solute diffusional exchange at the interface C_{ls}^d. In this work, the diffusional term C_{ls}^d is negligible. For the partitioning term C_{ls}^p two situations are considered: solidification and remelting. During solidification the solute mass transfer rate from the liquid to the solid without solute partitioning is $c_l \cdot M_{ls}$. However, due to partitioning the solid can only accept $k \cdot c_l \cdot M_{ls}$. The rest of solute $(1-k) \cdot c_l \cdot M_{ls}$ remains in the liquid, enriching solute in the melt. Therefore, we have $C_{ls}^p = c^* \cdot M_{ls}$ with $c^* = k \cdot c_l$ for solidification in Eq. (9). During remelting the solute mass transfer rate from solid to liquid is $c_s \cdot M_{sl}$. The solute mass is now completely accepted by the liquid. Therefore, we have $C_{sl}^p = c^* \cdot M_{sl}$ with $c^* = c_s$ for remelting in Eq. (9). Additionally, in order to predict the macrosegregation a mixture concentration is calculated with Eq. (11).

The energy conservation equations, Eq. (4), for both phases are solved separately. The exchange term $Q_{ls} (=-Q_{sl})$ is defined in Eq. (10). Two parts are included in the Q_{ls}: one due to phase change Q_{ls}^p and the other due to the liquid-solid interface heat transfer Q_{ls}^d. Our model assumes thermal equilibrium, i.e. $T_l = T_s$. To ensure this equilibrium a very large heat transfer coefficient ($H^* = 10^9 W/m^3/K$) between the liquid and the solid is applied. To handle the term Q_{ls}^p, solidification and remelting are also considered separately. During solidification the enthalpy per unit volume and time which should be transferred from the liquid to the solid is $h_l \cdot M_{ls}$. Referring to Eq. (10) we thus have $Q_{ls}^p = h^* \cdot M_{ls}$ with $h^* = h_l$. By analogy we have $Q_{sl}^p = h^* \cdot M_{sl}$ with $h^* = h_s$ for melting. At the same temperature the liquid enthalpy, h_l, is higher than the solid enthalpy, h_s. The enthalpy difference ($h_l - h_s = \Delta h_f$) defines the latent heat. The transfer of Q_{ls}^p does not change h_l directly, but forces h_s to increase, hence cause the solid temperature to rise locally. With the precondition of thermal equilibrium ($T_l = T_s$), the temperatures of the liquid and solid are balanced through volume heat exchange rate (H^*) between the phases. Test simulations showed that for large H^* the simulation results are independent of H^*. We therefore used a suitably large value of $H^*=10^9$ W·m^{-2}·K^{-1}. With this parameter the precondition of thermal equilibrium is maintained and the numerical results are stable.

Grain conservation is formulated in Eq. (5). The grain density n is transported according to the solid velocity. The source term N, namely the grain production rate, is defined in Eq. (6), and described in the following section.

Nucleation and Grain Transport

To describe the nucleation event in the presence of melt convection and grain movement the pragmatic approach originally developed by Oldfield[31] was used. This approach is based on the assumption that many potential nucleation sites exist in the melt, e.g. the inoculant particles through grain refiner. The nucleation sites belong to different families. Each family can only be activated as newly nucleated grains when a corresponding undercooling ΔT is achieved. The undercooling ΔT is defined as $T_f + m \cdot c_l - T$. The undercooling ΔT serves as the only driving force for nucleation. A Gaussian distribution describes the statistical outcome of all families of nucleation sites $dn/(d\Delta T)$. The three parameter for the Gaussian distribution are the mean nucleation undercooling corresponding to the maximum of the distribution, ΔT_N, the standard deviation of the distribution, ΔT_σ, and the maximum density of nuclei, n_{max}, given by the integral of the total distribution from zero to infinite undercooling. According to Rappaz[26], these three parameters can be determined experimentally for each melt by measuring the grain density (i.e. the grain size) and the corresponding maximum undercooling at recalescence, ΔT_{max}.

In order to apply the nucleation law in the numerical model, N in Eq. (5) is defined as $dn/(d(\Delta T)) \cdot d(\Delta T)/dt$. Because nucleation can occur in a partially solidified volume element, an Avrami-factor f_l is additionally considered in Eq. (6).

Grain Growth and Mass Transfer

As grains nucleate they start to grow. The Ti-inoculated Al-4 wt.% Cu alloy solidifies with a near globular equiaxed rather than a distinct dendritic morphology. The average diameter, d_s, of the grains can be determined from the fraction solid, f_s, and the grain density, n, according to Eq. (12). As the grains grow the solute element piles up ($k<1$) in front of the liquid-solid interface due to solute partitioning. The enriched solute is locally removed from the interface region towards the bulk melt by diffusion. Therefore, the concentration difference Δc between c_l^e (concentration in the melt at the interface) and c_l (concentration in the bulk melt) is taken as the driving force for solidification. With the assumption of thermodynamic equilibrium at the liquid-solid interface c_l^e can be determined from the local temperature T, i.e. $c_l^e = (T - T_f)/m$ according to the phase diagram. c_l is calculated from the solute conservation equation Eq. (3).

In addition to the driving force term Δc, M_{ls} is proportional to the overall solid-liquid interface area. Thus, it depends on the grain density n and the grain surface area πd_s^2, Eq. (7). The term f_l is the Avrami-factor. All other factors influencing the solidification rate are gathered in the empirical constant g_α (mm/s). g_α is named here as the 'growth factor'.

Numerical Implementation

The conservation equations Eq. (1) - (5) are numerically solved with a control-volume based finite difference method. A CFD software FLUENT version 4.5.6 is used. Both the liquid and solid share a single pressure field p. The pressure correction equation is obtained from the sum of the normalised mass continuity equations Eq. (1) using an extended SIMPLE algorithm[32]. For each time step, up to 60 iterations were necessarily made to decrease the normalised residual of c_l, c_s, f_s, $\vec{u}_l$, $\vec{u}_s$, p and n below the convergence limit 10^{-4}, and h_l and h_s below 10^{-6}. On each iteration the auxiliary quantities d_s and μ_s are updated first. We then calculated the exchange terms U_{ls}, C_{ls}, Q_{ls} and the source term N and M_{ls} based on the last iteration, and finally solved the conservation equations of momentum, mass, enthalpy and species.

FLUENT formulation is fully implicit. Theoretically there is no stability criterion that needs to be met in determining Δt. However, the time steps used impact the accuracy, and hence the reliability of the numerical results. Due to the complexity of the coupling there is no direct formulation to determine the optimal Δt. In the program an automatic Δt controller is integrated: If more than 40 iterations are needed to meet the convergence criterion, the program will reduce Δt. If in less than 20 iterations converge is met, then a larger Δt is used.

Results and Discussion

Description of the Studied Case

In order to demonstrate the abilities of the present model, we consider the 2D ingot casting with the calculation domain meshed into 40x40 square volume elements. The size of each element is

solute diffusional exchange at the interface C_{ls}^d. In this work, the diffusional term C_{ls}^d is negligible. For the partitioning term C_{ls}^p two situations are considered: solidification and remelting. During solidification the solute mass transfer rate from the liquid to the solid without solute partitioning is $c_l \cdot M_{ls}$. However, due to partitioning the solid can only accept $k \cdot c_l \cdot M_{ls}$. The rest of solute $(1-k) \cdot c_l \cdot M_{ls}$ remains in the liquid, enriching solute in the melt. Therefore, we have $C_{ls}^p = c^* \cdot M_{ls}$ with $c^* = k \cdot c_l$ for solidification in Eq. (9). During remelting the solute mass transfer rate from solid to liquid is $c_s \cdot M_{sl}$. The solute mass is now completely accepted by the liquid. Therefore, we have $C_{sl}^p = c^* \cdot M_{sl}$ with $c^* = c_s$ for remelting in Eq. (9). Additionally, in order to predict the macrosegregation a mixture concentration is calculated with Eq. (11).

The energy conservation equations, Eq. (4), for both phases are solved separately. The exchange term $Q_{ls}(=-Q_{sl})$ is defined in Eq. (10). Two parts are included in the Q_{ls}: one due to phase change Q_{ls}^p and the other due to the liquid-solid interface heat transfer Q_{ls}^d. Our model assumes thermal equilibrium, i.e. $T_l = T_s$. To ensure this equilibrium a very large heat transfer coefficient ($H^* = 10^9 W/m^3/K$) between the liquid and the solid is applied. To handle the term Q_{ls}^p, solidification and remelting are also considered separately. During solidification the enthalpy per unit volume and time which should be transferred from the liquid to the solid is $h_l \cdot M_{ls}$. Referring to Eq. (10) we thus have $Q_{ls}^p = h^* \cdot M_{ls}$ with $h^* = h_l$. By analogy we have $Q_{sl}^p = h^* \cdot M_{sl}$ with $h^* = h_s$ for melting. At the same temperature the liquid enthalpy, h_l, is higher than the solid enthalpy, h_s. The enthalpy difference $(h_l - h_s = \Delta h_f)$ defines the latent heat. The transfer of Q_{ls}^p does not change h_l directly, but forces h_s to increase, hence cause the solid temperature to rise locally. With the precondition of thermal equilibrium ($T_l = T_s$), the temperatures of the liquid and solid are balanced through volume heat exchange rate (H^*) between the phases. Test simulations showed that for large H^* the simulation results are independent of H^*. We therefore used a suitably large value of $H^* = 10^9$ W·m⁻²·K⁻¹. With this parameter the precondition of thermal equilibrium is maintained and the numerical results are stable.

Grain conservation is formulated in Eq. (5). The grain density n is transported according to the solid velocity. The source term N, namely the grain production rate, is defined in Eq. (6), and described in the following section.

Nucleation and Grain Transport

To describe the nucleation event in the presence of melt convection and grain movement the pragmatic approach originally developed by Oldfield[31] was used. This approach is based on the assumption that many potential nucleation sites exist in the melt, e.g. the inoculant particles through grain refiner. The nucleation sites belong to different families. Each family can only be activated as newly nucleated grains when a corresponding undercooling ΔT is achieved. The undercooling ΔT is defined as $T_f + m \cdot c_l - T$. The undercooling ΔT serves as the only driving force for nucleation. A Gaussian distribution describes the statistical outcome of all families of nucleation sites $dn/(d\Delta T)$. The three parameter for the Gaussian distribution are the mean nucleation undercooling corresponding to the maximum of the distribution, ΔT_N, the standard deviation of the distribution, ΔT_σ, and the maximum density of nuclei, n_{max}, given by the integral of the total distribution from zero to infinite undercooling. According to Rappaz[26], these three parameters can be determined experimentally for each melt by measuring the grain density (i.e. the grain size) and the corresponding maximum undercooling at recalescence, ΔT_{max}.

In order to apply the nucleation law in the numerical model, N in Eq. (5) is defined as $dn/(d(\Delta T)) \cdot d(\Delta T)/dt$. Because nucleation can occur in a partially solidified volume element, an Avrami-factor f_l is additionally considered in Eq. (6).

Grain Growth and Mass Transfer

As grains nucleate they start to grow. The Ti-inoculated Al-4 wt.% Cu alloy solidifies with a near globular equiaxed rather than a distinct dendritic morphology. The average diameter, d_s, of the grains can be determined from the fraction solid, f_s, and the grain density, n, according to Eq. (12). As the grains grow the solute element piles up ($k<1$) in front of the liquid-solid interface due to solute partitioning. The enriched solute is locally removed from the interface region towards the bulk melt by diffusion. Therefore, the concentration difference Δc between c_l^e (concentration in the melt at the interface) and c_l (concentration in the bulk melt) is taken as the driving force for solidification. With the assumption of thermodynamic equilibrium at the liquid-solid interface c_l^e can be determined from the local temperature T, i.e. $c_l^e = (T - T_f)/m$ according to the phase diagram. c_l is calculated from the solute conservation equation Eq. (3).

In addition to the driving force term Δc, M_{ls} is proportional to the overall solid-liquid interface area. Thus, it depends on the grain density n and the grain surface area πd_s^2, Eq. (7). The term f_l is the Avrami-factor. All other factors influencing the solidification rate are gathered in the empirical constant g_α (mm/s). g_α is named here as the 'growth factor'.

Numerical Implementation

The conservation equations Eq. (1) - (5) are numerically solved with a control-volume based finite difference method. A CFD software FLUENT version 4.5.6 is used. Both the liquid and solid share a single pressure field p. The pressure correction equation is obtained from the sum of the normalised mass continuity equations Eq. (1) using an extended SIMPLE algorithm[32]. For each time step, up to 60 iterations were necessarily made to decrease the normalised residual of c_l, c_s, f_s, $\bar{u}_l$, $\bar{u}_s$, p and n below the convergence limit 10^{-4}, and h_l and h_s below 10^{-6}. On each iteration the auxiliary quantities d_s and μ_s are updated first. We then calculated the exchange terms U_{ls}, C_{ls}, Q_{ls} and the source term N and M_{ls} based on the last iteration, and finally solved the conservation equations of momentum, mass, enthalpy and species.

FLUENT formulation is fully implicit. Theoretically there is no stability criterion that needs to be met in determining Δt. However, the time steps used impact the accuracy, and hence the reliability of the numerical results. Due to the complexity of the coupling there is no direct formulation to determine the optimal Δt. In the program an automatic Δt controller is integrated: If more than 40 iterations are needed to meet the convergence criterion, the program will reduce Δt. If in less than 20 iterations converge is met, then a larger Δt is used.

Results and Discussion

Description of the Studied Case

In order to demonstrate the abilities of the present model, we consider the 2D ingot casting with the calculation domain meshed into 40x40 square volume elements. The size of each element is

5x5 mm². The finer the volume elements, the smaller the time step necessary to meet the convergence criterion, and hence the higher the calculation cost. In the simulations presented below the automatic time step controller was activated. At the initial stage of solidification we have started with $\Delta t = 2 \times 10^{-4}$ s, while in the later stage it is then automatically increased to 1×10^{-3} s. A single simulation run took 2 weeks on a SGI Octane workstation (MIPS R12000).

The casting is supposed to be filled instantaneously. Cooling starts from an initial temperature of 925 K. The surrounding mold (not modeled explicitly) is kept at a constant temperature of 290 K. A heat transfer coefficient H at the casting/mold interface is introduced and assumed to be 750 W/(m²K). For both the liquid and the solid convection, we assume a non-slip boundary condition at the mould.

The recent model did not consider a free surface formed at the top of the casting. Therefore, we applied a special boundary condition with constant temperature, constant concentration and constant pressure at the top inlet, and considered the side wall of the inlet to be thermally isolated. During solidification hot melt from the inlet continuously feeds the solidification shrinkage.

Table II. Thermophysical and thermodynamic properties used for the simulation		
$\rho_l = 2606$ kg·m⁻¹	$c_{p(l)} = 1179$ J·kg⁻¹·K⁻¹	$\mu_l = 1.3 \times 10^{-2}$ kg·m⁻¹·s⁻¹
$\rho_s = 2743$ kg·m⁻¹	$c_{p(s)} = 766$ J·kg⁻¹·K⁻¹	$T_f = 933.5$ K
$k_l = 77$ W·m⁻¹·K⁻¹	$D_l^{Cu} = 5 \times 10^{-9}$ m²·s⁻¹	$k = 0.145$
$k_s = 153$ W·m⁻¹·K⁻¹	$D_s^{Cu} = 8 \times 10^{-13}$ m²·s⁻¹	$m = -344$ K

We selected an inoculated Al-4 wt.% Cu alloy because of its almost globular equiaxed solidification morphology. Table II shows the physical properties and phase diagram parameters of this alloy. The density of the liquid and solid are assumed to be constant but different, and therefore, the thermal solutal convection is not taken into account. The parameters used for the nucleation law were $n_{max} = 10^{14}$ m⁻³, $\Delta T_N = 10$ K, $\Delta T_\sigma = 4$ K. As initial grain diameter we assume $d_s = 1$ µm and for the 'growth factor' $g_\alpha = 5 \cdot 10^{-4}$ m/s.

Numerical Predictions

Fig. 1a shows that both the isotherm and solidification isoline are symmetrical in the initial stage, and the solidification process is dominated by the heat extraction of the mold. As soon as T drops below the liquidus, nucleation ($N > 0$) and solidification ($M_{ls} > 0$) start, first in the four corners, and subsequently along the mould walls. The solid forming directly on the wall does not move. The first reason for this is the applied non-slip boundary condition: the grains that nucleate on the surface are supposed to be adhered to the wall. The second reason is that the local solidification rate at the surface and the corner regions is so high that a rigid shell (the fraction solid reaches the packing limit) forms in a couple of seconds. With the increasing f_s in the corners the melt becomes enriched in solute c_l. In the initial stage the grain sedimentation and the sedimentation caused convection are not significant, but the feeding flow is strong. This feeding flow is caused by solidification shrinkage and depends on the integrated mass transfer rate.

With further solidification (Fig. 1b) those solid grains which are not directly adhered to mold wall sink downwards. As the solid and the liquid are coupled through the momentum exchange terms, the melt is drawn by sinking solid. Two vortices occur in the bulk melt - one clockwise in the right half and one anticlockwise in the left haft of the casting. The packing limit is exceeded in the four corner regions and the packing solid forms a rigid porous body there. Sedimentation leads to the accumulation of solid mainly at the bottom corners, but also along the bottom itself. Due to this sedimentation the f_s isolines at the lower bottom regions proceed faster than in the side wall regions. For $f_s < f_s^c = 0.637$ (packing limit) the solid and the liquid move in a similar manner along the two vortices. The flow currents become so strong that they carry the solid upwards towards the hot center of the casting, causing the solid to melt. In a later stage of the solidification process, the grain density in the corner regions and along the mould walls remains almost unchanged. However, new grains nucleate in the bulk melt. As soon as the grains nucleate they quickly grow to an average size of around 50 µm, the largest in the middle bottom region, where the solid volume fraction is between 0.3-0.5.

a)

T: 876~925 K	M_{ls}:0~180 kg/m³/s	f_s: 0~0.77	$\bar{u}_{s,max}$ =0.38 mm/s	d_s: 0~40 µm

b)

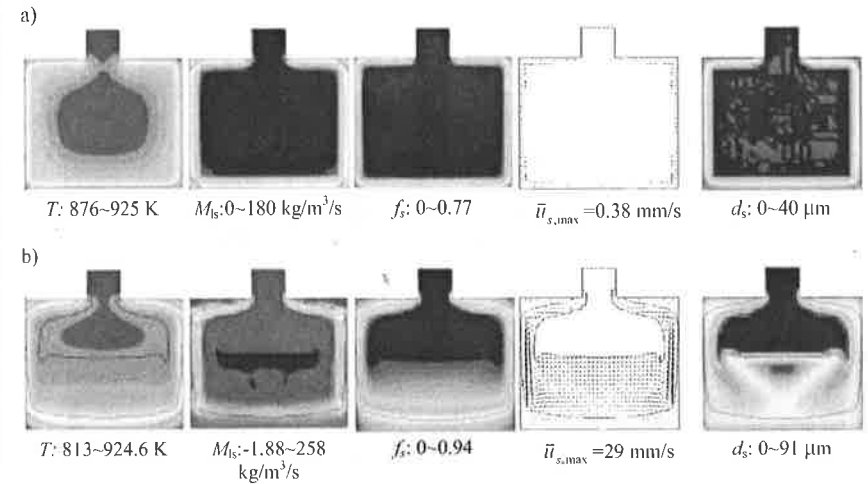|				
T: 813~924.6 K	M_{ls}:-1.88~258 kg/m³/s	f_s: 0~0.94	$\bar{u}_{s,max}$ =29 mm/s	d_s: 0~91 µm

Fig. 1: Simulation results a) 8s and b) 35s after the cooling has started. The arrows of both velocity fields are continuously scaled starting from zero to the maximum value given. All the other quantities are scaled equidistantly by 30 colors, with blue representing the lowest and red the highest value. The minimum and the maximum values are given below the corresponding picture. Two fraction solid iso-lines (0.01 and 0.64) are drawn together with each figure of b).

Fig. 2 shows the complexity of macrosegregation formation. Different segregation regions are marked with **A-D**. First segregations appear in the lower corner regions about 10 s after the cooling has started. The negative segregations **A** ($c_{mix} < 4\%$) are caused by the sedimentation. The solute poor grains sink along the wall and settle there as the local fraction solid exceeds the packing limit $f_s^c = 0.637$. According to Eq. (11), the mixed concentration c_{mix} is determined

5x5 mm². The finer the volume elements, the smaller the time step necessary to meet the convergence criterion, and hence the higher the calculation cost. In the simulations presented below the automatic time step controller was activated. At the initial stage of solidification we have started with $\Delta t = 2 \times 10^{-4}$ s, while in the later stage it is then automatically increased to 1×10^{-3} s. A single simulation run took 2 weeks on a SGI Octane workstation (MIPS R12000).

The casting is supposed to be filled instantaneously. Cooling starts from an initial temperature of 925 K. The surrounding mold (not modeled explicitly) is kept at a constant temperature of 290 K. A heat transfer coefficient H at the casting/mold interface is introduced and assumed to be 750 W/(m²K). For both the liquid and the solid convection, we assume a non-slip boundary condition at the mould.

The recent model did not consider a free surface formed at the top of the casting. Therefore, we applied a special boundary condition with constant temperature, constant concentration and constant pressure at the top inlet, and considered the side wall of the inlet to be thermally isolated. During solidification hot melt from the inlet continuously feeds the solidification shrinkage.

Table II. Thermophysical and thermodynamic properties used for the simulation		
$\rho_l = 2606$ kg·m^{-1}	$c_{p(l)} = 1179$ J·kg^{-1}·K^{-1}	$\mu_l = 1.3 \times 10^{-2}$ kg·m^{-1}·s^{-1}
$\rho_s = 2743$ kg·m^{-1}	$c_{p(s)} = 766$ J·kg^{-1}·K^{-1}	$T_f = 933.5$ K
$k_l = 77$ W·m^{-1}·K^{-1}	$D_l^{Cu} = 5 \times 10^{-9}$ m²·s^{-1}	$k = 0.145$
$k_s = 153$ W·m^{-1}·K^{-1}	$D_s^{Cu} = 8 \times 10^{-13}$ m²·s^{-1}	$m = -344$ K

We selected an inoculated Al-4 wt.% Cu alloy because of its almost globular equiaxed solidification morphology. Table II shows the physical properties and phase diagram parameters of this alloy. The density of the liquid and solid are assumed to be constant but different, and therefore, the thermal solutal convection is not taken into account. The parameters used for the nucleation law were $n_{max} = 10^{14}$ m^{-3}, $\Delta T_N = 10$ K, $\Delta T_\sigma = 4$ K. As initial grain diameter we assume $d_s = 1$ µm and for the 'growth factor' $g_\alpha = 5 \cdot 10^{-4}$ m/s.

Numerical Predictions

Fig. 1a shows that both the isotherm and solidification isoline are symmetrical in the initial stage, and the solidification process is dominated by the heat extraction of the mold. As soon as T drops below the liquidus, nucleation ($N > 0$) and solidification ($M_{ls} > 0$) start, first in the four corners, and subsequently along the mould walls. The solid forming directly on the wall does not move. The first reason for this is the applied non-slip boundary condition: the grains that nucleate on the surface are supposed to be adhered to the wall. The second reason is that the local solidification rate at the surface and the corner regions is so high that a rigid shell (the fraction solid reaches the packing limit) forms in a couple of seconds. With the increasing f_s in the corners the melt becomes enriched in solute c_l. In the initial stage the grain sedimentation and the sedimentation caused convection are not significant, but the feeding flow is strong. This

feeding flow is caused by solidification shrinkage and depends on the integrated mass transfer rate.

With further solidification (Fig. 1b) those solid grains which are not directly adhered to mold wall sink downwards. As the solid and the liquid are coupled through the momentum exchange terms, the melt is drawn by sinking solid. Two vortices occur in the bulk melt - one clockwise in the right half and one anticlockwise in the left haft of the casting. The packing limit is exceeded in the four corner regions and the packing solid forms a rigid porous body there. Sedimentation leads to the accumulation of solid mainly at the bottom corners, but also along the bottom itself. Due to this sedimentation the f_s isolines at the lower bottom regions proceed faster than in the side wall regions. For $f_s < f_s^c = 0.637$ (packing limit) the solid and the liquid move in a similar manner along the two vortices. The flow currents become so strong that they carry the solid upwards towards the hot center of the casting, causing the solid to melt. In a later stage of the solidification process, the grain density in the corner regions and along the mould walls remains almost unchanged. However, new grains nucleate in the bulk melt. As soon as the grains nucleate they quickly grow to an average size of around 50 µm, the largest in the middle bottom region, where the solid volume fraction is between 0.3-0.5.

a)

| T: 876~925 K | M_{ls}:0~180 kg/m³/s | f_s: 0~0.77 | $\bar{u}_{s,max} = 0.38$ mm/s | d_s: 0~40 µm |

b)

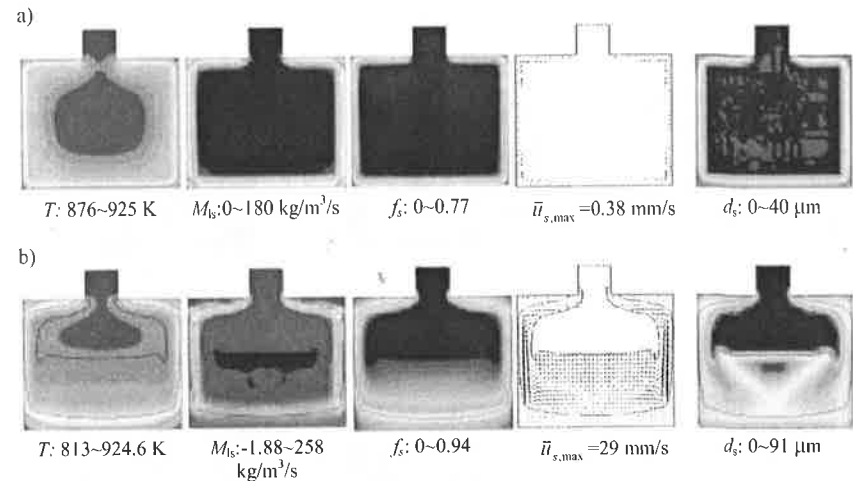| T: 813~924.6 K | M_{ls}:-1.88~258 kg/m³/s | f_s: 0~0.94 | $\bar{u}_{s,max} = 29$ mm/s | d_s: 0~91 µm |

Fig. 1: Simulation results a) 8s and b) 35s after the cooling has started. The arrows of both velocity fields are continuously scaled starting from zero to the maximum value given. All the other quantities are scaled equidistantly by 30 colors, with blue representing the lowest and red the highest value. The minimum and the maximum values are given below the corresponding picture. Two fraction solid iso-lines (0.01 and 0.64) are drawn together with each figure of b).

Fig. 2 shows the complexity of macrosegregation formation. Different segregation regions are marked with A-D. First segregations appear in the lower corner regions about 10 s after the cooling has started. The negative segregations A ($c_{mix} < 4\%$) are caused by the sedimentation. The solute poor grains sink along the wall and settle there as the local fraction solid exceeds the packing limit $f_s^c = 0.637$. According to Eq. (11), the mixed concentration c_{mix} is determined

by α_s, α_l, c_l and c_s. As c_s is much lower than the $c_l (k < 1)$, regions with higher grain settlement rate have lower mixed concentration c_{mix}. The positive segregation zone **C** just close to **A** at the lower corner is caused by melt flow. As the grains settle in zone **A**, solute-enriched melt has to leave this region in order to provide space for the settling grains. This solute-enriched melt is squeezed out from region **A** so that the positive segregation zone **C** forms just near to it. More details about this mechanism are shown in Fig. 3a-c (see below). This positive resegregation forms temporally in the bulk melt, and will move with the melt flow while solidification proceeds.

Similarly negative segregations **A** form near the top corners. Again grain sedimentation is the origin of their formation. $\bar{u}_s$ field shows that the grains nucleated near the upper wall tend to move towards the corner. The grains moving towards the corner cause the local fraction solid to increase. As f_s exceeds the packing limit, $\bar{u}_s$ vanishes and the oncoming grains settle here and hence negative segregations form. However, in the late stage of solidification these negative segregated zones **A** seem to "move" gradually downwards. As the local f_s exceeds the packing limit the oncoming grains settle and broaden the negative segregation zones while the melt penetrates through the voids between the packed grains to feed the solidification shrinkage. The solute-enriched feeding melt can partially level out the negative segregation near the casting wall so that the negative segregation becomes weaker.
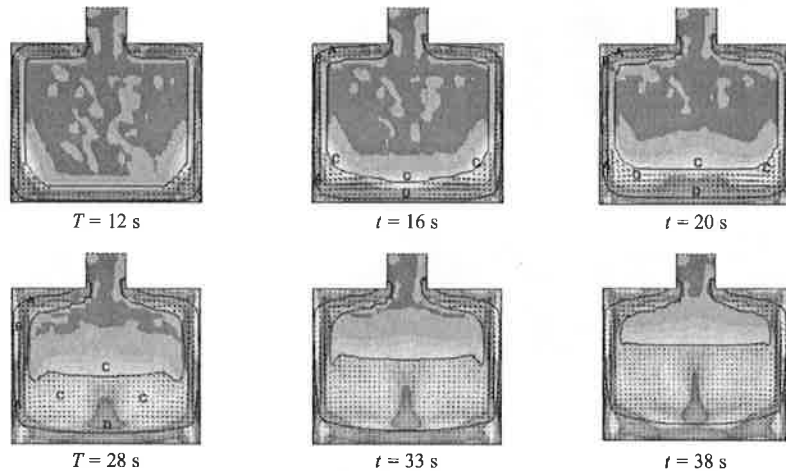

$T = 12$ s $t = 16$ s $t = 20$ s

$T = 28$ s $t = 33$ s $t = 38$ s

Fig. 2: Sequence of macrosegregation pattern (c_{mix}) overlaid with the velocity of the solid phase. The arrows of each velocity field are continuously scaled starting from zero to the maximum value. c_{mix} is scaled with 30 colors, with blue representing the lowest (3.7%) and yellow the highest value (4.3%). Two fraction solid iso-lines (0.01 and 0.64) are drawn together with each figure

The positive segregation area **B** just below the upper corners are also produced by grain movement. A gradient in solid velocity is present in front of zones **B**. The grains at the corner cannot move. However, just below the corner when the local fraction solid is still smaller than the packing limit the grains start to sink. Thus, grains can leave the region **B** before the packing limit is exceeded. The volume of the exiting grains must be filled by the solute-enriched melt.

The direct outcome of this phase transport phenomenon, i.e. the depletion of the solute poor solid and the feeding by the solute-enriched melt, is the increase of the local mixed concentration c_{mix}.

At $t = 16$ s a negative segregated area **D** occurs on the lower bottom wall near the area of $f_s > f_s^c = 0.637$ caused again by the grain sedimentation. This lower concentration area **D** results in a corresponding higher concentration area **C** located directly at the outer boundary of the mushy zone. As solidification proceeds, the three higher concentration areas **C** located at the outer boundary of the mushy zone (labeled **C** in **Fig. 2**) are not stationary. They move with the flow currents and ascends towards the inner regions of the casting.

a) melt convection (max $\bar{u}_l$=7.29 mm/s) and f_s d) Feeding flow (max $\bar{u}_l$=0.3 mm/s) and f_s

b) Convective flow in the lower corner   e) feeding flow in the lower corner

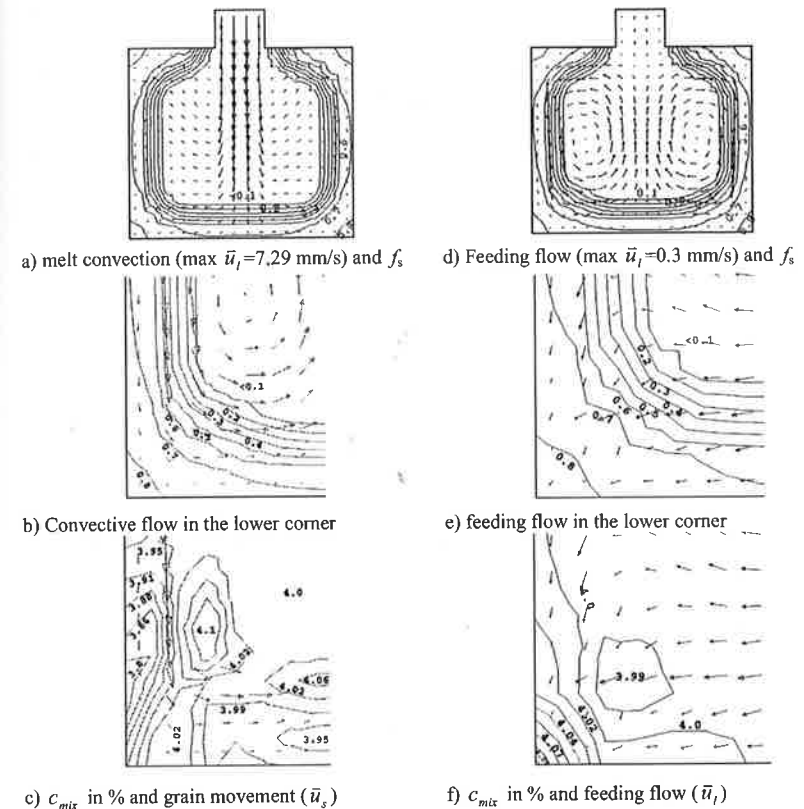c) c_{mix} in % and grain movement ($\bar{u}_s$)   f) c_{mix} in % and feeding flow ($\bar{u}_l$)

Fig. 3: Influence of grain sedimentation and melt flow on macrosegregation formation ($\Delta t = 20$ s). considering flow induced by solidification shrinkage and movement of grains (a-c); and considering shrinkage flow alone (d-f).

In order to stress the influence of shrinkage flow (feeding flow) on macrosegregation, a artificial case without grain movement is simulated (Fig. 3d-f) and compared to the normal case of the equiaxed solidification with grain movement (Fig. 3a-c). In case of no grain movement the

by α_s, α_l, c_l and c_s. As c_s is much lower than the $c_l (k < 1)$, regions with higher grain settlement rate have lower mixed concentration c_{mix}. The positive segregation zone **C** just close to **A** at the lower corner is caused by melt flow. As the grains settle in zone **A**, solute-enriched melt has to leave this region in order to provide space for the settling grains. This solute-enriched melt is squeezed out from region **A** so that the positive segregation zone **C** forms just near to it. More details about this mechanism are shown in Fig. 3a-c (see below). This positive re-segregation forms temporally in the bulk melt, and will move with the melt flow while solidification proceeds.

Similarly negative segregations **A** form near the top corners. Again grain sedimentation is the origin of their formation. $\bar{u}_s$ field shows that the grains nucleated near the upper wall tend to move towards the corner. The grains moving towards the corner cause the local fraction solid to increase. As f_s exceeds the packing limit, $\bar{u}_s$ vanishes and the oncoming grains settle here and hence negative segregations form. However, in the late stage of solidification these negative segregated zones **A** seem to "move" gradually downwards. As the local f_s exceeds the packing limit the oncoming grains settle and broaden the negative segregation zones while the melt penetrates through the voids between the packed grains to feed the solidification shrinkage. The solute-enriched feeding melt can partially level out the negative segregation near the casting wall so that the negative segregation becomes weaker.
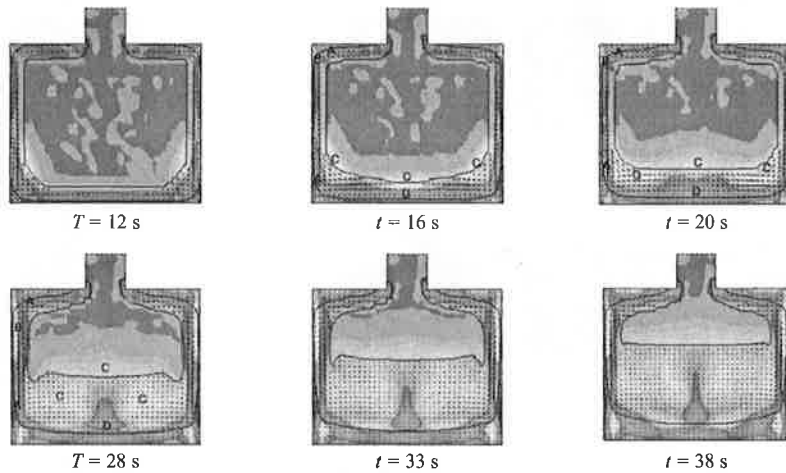

$T = 12$ s $t = 16$ s $t = 20$ s

$T = 28$ s $t = 33$ s $t = 38$ s

Fig. 2: Sequence of macrosegregation pattern (c_{mix}) overlaid with the velocity of the solid phase. The arrows of each velocity field are continuously scaled starting from zero to the maximum value. c_{mix} is scaled with 30 colors, with blue representing the lowest (3.7%) and yellow the highest value (4.3%). Two fraction solid iso-lines (0.01 and 0.64) are drawn together with each figure

The positive segregation area **B** just below the upper corners are also produced by grain movement. A gradient in solid velocity is present in front of zones **B**. The grains at the corner cannot move. However, just below the corner when the local fraction solid is still smaller than the packing limit the grains start to sink. Thus, grains can leave the region **B** before the packing limit is exceeded. The volume of the exiting grains must be filled by the solute-enriched melt.

The direct outcome of this phase transport phenomenon, i.e. the depletion of the solute poor solid and the feeding by the solute-enriched melt, is the increase of the local mixed concentration c_{mix}.

At $t = 16$ s a negative segregated area **D** occurs on the lower bottom wall near the area of $f_s > f_s^c = 0.637$ caused again by the grain sedimentation. This lower concentration area **D** results in a corresponding higher concentration area **C** located directly at the outer boundary of the mushy zone. As solidification proceeds, the three higher concentration areas **C** located at the outer boundary of the mushy zone (labeled **C** in **Fig. 2**) are not stationary. They move with the flow currents and ascends towards the inner regions of the casting.

a) melt convection (max $\bar{u}_l$=7.29 mm/s) and f_s

d) Feeding flow (max $\bar{u}_l$=0.3 mm/s) and f_s

b) Convective flow in the lower corner

e) feeding flow in the lower corner

c) c_{mix} in % and grain movement ($\bar{u}_s$)
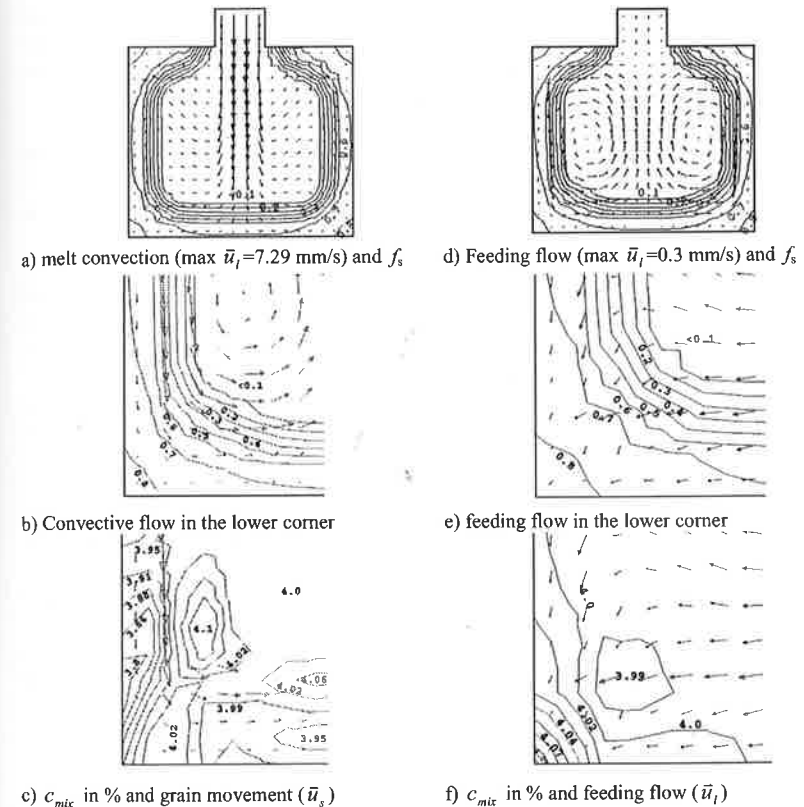
f) c_{mix} in % and feeding flow ($\bar{u}_l$)

Fig. 3: Influence of grain sedimentation and melt flow on macrosegregation formation ($\Delta t = 20$ s). considering flow induced by solidification shrinkage and movement of grains (a-c); and considering shrinkage flow alone (d-f).

In order to stress the influence of shrinkage flow (feeding flow) on macrosegregation, a artificial case without grain movement is simulated (Fig. 3d-f) and compared to the normal case of the equiaxed solidification with grain movement (Fig. 3a-c). In case of no grain movement the

solid phase, i.e. the grains, is supposed to be stationary; the solidification induced shrinkage ($\rho_s > \rho_l$) leads to feeding flow and the solid viscosity is set to infinitely. The flow pattern of the case with and without grain movement is totally different. The flow pattern shown in Fig. 3d is caused only by the solidification shrinkage, while the flow pattern shown in Fig. 3a is attributed to both the solidification shrinkage and the flow dragged by the moving (sinking) grains.

The development of macrosegregation is strongly influenced by grain movement. In case of no grain movement (Fig. 3e-f), the penetrating flow carries the solute enriched melt to feed the solidification shrinkage. Thus, positive segregation develops in the corner where the solidification starts in our simple geometry. However, with grain movement (Fig. 3b-c) both, the liquid convection and the grain migration/settlement contribute to the development of macrosegregation. Because of a high grain settlement rate, regions facing the oncoming grains have negative segregation,. Regions from which grains are carried away by the convection reveal positive segregation, because the space of the leaving grains is fed generally by the solute enriched melt.

Although the numerical predictions are quite helpful in understanding the different interactions occurring in solidification with convection, we have to regret that the presented simulation results have not yet been compared with experiment. Before doing so, following points needs to be further worked on:

- The model can not handle free surfaces. However shrinkage cavities may form at the casting top or in the casting center. Therefore, an idealizing boundary condition at the casting top, i.e. pressure inlet, is applied: Hot melt is assume to flow through the inlet to feed the casting continuously. This lead to the somewhat unrealistic situation that the casting can never completely solidify.
- Only sedimentation induced flow and shrinkage flow are considered here. Thermosolutal convection is ignored. Thermosolutal convection would of cause influence the general flow pattern and the macrosegregation distribution consequently.
- The parameters used for the nucleation law and grain growth are critical for the calculation of the grain density and grain diameter. Experimental casting trials for the investigated alloy and statistical analyses[1,17] must first be undertaken to determine those parameters.

Despite of the simplifications the recent numerical model provides an effective method to study the globular equiaxed solidification process and the development of macrosegregations. Some hypotheses and theories were achieved in last decades for the explanation of macrostructure and macrosegregation formation[1-3], but it is difficult to use those ideas to explain the results in the real castings, because the complicated nucleation and grain growth processes, convection, grain movement, solute transportation, etc. are not to be observed. The numerical model offers the possibility to 'visualize' all those details.

Conclusions

The presented model is able to simulate globular equiaxed solidification including nucleation, grain evolution, melt convection, sedimentation, solute transport and macrosegregation formation. It is an effective method of coupling the macroscopic solidification processes with microscopic phenomena. By analyzing the simulation results for the solidification of an Al-4wt%Cu ingot casting, deep understanding on the following features could be achieved.

- Due to heat extraction grains initially nucleate in the vicinity of the mould wall. As their density is higher than the surrounding melt, those grains with no direct contact to the mould wall start to sink.
- The sinking of grains produces a downward melt flow along the mould wall and a corresponding upward flow in the middle of the casting.
- Sinking grains partly settle at the bottom of the casting and partly flow with the melt current into the bulk melt. Here remelting occurs. However, we did not predict any grain dissolution.
- Grain settlement always results in negative macrosegregation. We predict grain settlement (i) in the upper corners, (ii) at the bottom of vertical walls, and (iii) at the bottom in the middle of the casting.
- Positive macrosegregations found in this paper may form for 3 reasons (i) depletion of grains and the corresponding inward flow with segregated melt, (ii) feeding flow, and (iii) squeezing out of segregated melt by settling grains. Areas of positive macrosegregation caused by (iii) are mainly liquid and thus may move during the course of solidification. Those caused by (i) and (ii) do not move.
- Feeding flow with segregated melt into areas with large solid fraction reduces negative and increases positive macrosegregation.

Acknowledgements

References

1. M.C. Flemings, *Solidification processing* (New York, NY: McGraw-Hill, 1974).
2. J. Campbell, *Castings* (Oxford: Butterworth-Heinemann Ltd, 1991).
3. A. Ohno, *Solidification:The separation theory and its practical applications* (Berlin: Springer-Verlag, 1987).
4. W.D. Bennon and F.P. Incropera, "A continuum model for momentum, heat and species transport in binary solid-liquid phase change systems – I. Model formulation," *Intern. J. Heat Mass Transfer,* 30(1987), 2161-2170.
5. V.R. Voller and C. Prakash, "A fixed grid numerical modeling methodology for convection-diffusion mushy region phase-change problems," *Intern. J. Heat Mass Transfer*, 30(1987), 1709-1719.
6. Q.Z. Diao and H.L. Tsai, "Modeling of the formation of under-riser macro-segregation during solidification of binary alloys," *Metall. Mater. Trans. A*, 25A(1994), 1051-1064.
7. J. Ni and F.P. Incropera, "Extension of the continuum model for transport phenomena occurring during metal alloy solidification – I. The conservation equations," *Intern. J. Heat Mass Transfer*, 38(1995), 1271-1284.
8. J. Ni and F.P. Incropera, "Extension of the continuum model for transport phenomena occurring during metal alloy solidification – II. Microscopic considerations," *Intern. J. Heat Mass Transfer*, 38(1995), 1285-1296.
9. C.J. Vreeman, M.J.M. Krane, and F.P. Incropera, "The effect of free-floating dendrites and convection on macro-segregation in direct cast aluminum alloys – I: model development," *Intern. J. Heat Mass Transfer*, 43(2000), 677-686.
10. C. J. Vreeman and F.P. Incropera, "The effect of free-floating dendrites and convection on macro-segregation in direct cast aluminum alloys – II: predictions for Al-Cu and Al-Mg alloys," *Intern. J. Heat Mass Transfer*, 43(2000), 697-704.

solid phase, i.e. the grains, is supposed to be stationary; the solidification induced shrinkage ($\rho_s > \rho_l$) leads to feeding flow and the solid viscosity is set to infinitely. The flow pattern of the case with and without grain movement is totally different. The flow pattern shown in Fig. 3d is caused only by the solidification shrinkage, while the flow pattern shown in Fig. 3a is attributed to both the solidification shrinkage and the flow dragged by the moving (sinking) grains.

The development of macrosegregation is strongly influenced by grain movement. In case of no grain movement (Fig. 3e-f), the penetrating flow carries the solute enriched melt to feed the solidification shrinkage. Thus, positive segregation develops in the corner where the solidification starts in our simple geometry. However, with grain movement (Fig. 3b-c) both, the liquid convection and the grain migration/settlement contribute to the development of macrosegregation. Because of a high grain settlement rate, regions facing the oncoming grains have negative segregation,. Regions from which grains are carried away by the convection reveal positive segregation, because the space of the leaving grains is fed generally by the solute enriched melt.

Although the numerical predictions are quite helpful in understanding the different interactions occurring in solidification with convection, we have to regret that the presented simulation results have not yet been compared with experiment. Before doing so, following points needs to be further worked on:

- The model can not handle free surfaces. However shrinkage cavities may form at the casting top or in the casting center. Therefore, an idealizing boundary condition at the casting top, i.e. pressure inlet, is applied: Hot melt is assume to flow through the inlet to feed the casting continuously. This lead to the somewhat unrealistic situation that the casting can never completely solidify.
- Only sedimentation induced flow and shrinkage flow are considered here. Thermosolutal convection is ignored. Thermosolutal convection would of cause influence the general flow pattern and the macrosegregation distribution consequently.
- The parameters used for the nucleation law and grain growth are critical for the calculation of the grain density and grain diameter. Experimental casting trials for the investigated alloy and statistical analyses[1,17] must first be undertaken to determine those parameters.

Despite of the simplifications the recent numerical model provides an effective method to study the globular equiaxed solidification process and the development of macrosegregations. Some hypotheses and theories were achieved in last decades for the explanation of macrostructure and macrosegregation formation[1-3], but it is difficult to use those ideas to explain the results in the real castings, because the complicated nucleation and grain growth processes, convection, grain movement, solute transportation, etc. are not to be observed. The numerical model offers the possibility to 'visualize' all those details.

Conclusions

The presented model is able to simulate globular equiaxed solidification including nucleation, grain evolution, melt convection, sedimentation, solute transport and macrosegregation formation. It is an effective method of coupling the macroscopic solidification processes with microscopic phenomena. By analyzing the simulation results for the solidification of an Al-4wt%Cu ingot casting, deep understanding on the following features could be achieved.

- Due to heat extraction grains initially nucleate in the vicinity of the mould wall. As their density is higher than the surrounding melt, those grains with no direct contact to the mould wall start to sink.
- The sinking of grains produces a downward melt flow along the mould wall and a corresponding upward flow in the middle of the casting.
- Sinking grains partly settle at the bottom of the casting and partly flow with the melt current into the bulk melt. Here remelting occurs. However, we did not predict any grain dissolution.
- Grain settlement always results in negative macrosegregation. We predict grain settlement (i) in the upper corners, (ii) at the bottom of vertical walls, and (iii) at the bottom in the middle of the casting.
- Positive macrosegregations found in this paper may form for 3 reasons (i) depletion of grains and the corresponding inward flow with segregated melt, (ii) feeding flow, and (iii) squeezing out of segregated melt by settling grains. Areas of positive macrosegregation caused by (iii) are mainly liquid and thus may move during the course of solidification. Those caused by (i) and (ii) do not move.
- Feeding flow with segregated melt into areas with large solid fraction reduces negative and increases positive macrosegregation.

References

1. M.C. Flemings, *Solidification processing* (New York, NY: McGraw-Hill, 1974).
2. J. Campbell, *Castings* (Oxford: Butterworth-Heinemann Ltd, 1991).
3. A. Ohno, *Solidification:The separation theory and its practical applications* (Berlin: Springer-Verlag, 1987).
4. W.D. Bennon and F.P. Incropera, "A continuum model for momentum, heat and species transport in binary solid-liquid phase change systems – I. Model formulation," *Intern. J. Heat Mass Transfer,* 30(1987), 2161-2170.
5. V.R. Voller and C. Prakash, "A fixed grid numerical modeling methodology for convection-diffusion mushy region phase-change problems," *Intern. J. Heat Mass Transfer,* 30(1987), 1709-1719.
6. Q.Z. Diao and H.L. Tsai, "Modeling of the formation of under-riser macro-segregation during solidification of binary alloys," *Metall. Mater. Trans. A,* 25A(1994), 1051-1064.
7. J. Ni and F.P. Incropera, "Extension of the continuum model for transport phenomena occurring during metal alloy solidification – I. The conservation equations," *Intern. J. Heat Mass Transfer,* 38(1995), 1271-1284.
8. J. Ni and F.P. Incropera, "Extension of the continuum model for transport phenomena occurring during metal alloy solidification – II. Microscopic considerations," *Intern. J. Heat Mass Transfer,* 38(1995), 1285-1296.
9. C.J. Vreeman, M.J.M. Krane, and F.P. Incropera, "The effect of free-floating dendrites and convection on macro-segregation in direct cast aluminum alloys – I: model development," *Intern. J. Heat Mass Transfer,* 43(2000), 677-686.
10. C. J. Vreeman and F.P. Incropera, "The effect of free-floating dendrites and convection on macro-segregation in direct cast aluminum alloys – II: predictions for Al-Cu and Al-Mg alloys," *Intern. J. Heat Mass Transfer,* 43(2000), 697-704.

11. H.J. Thevik, A. Mo, and T. Rusten, "A mathematical model for surface segregation in aluminum direct chill casting," *Metall. Mater. Trans. B*, 30B(1999), 135-142.
12. C. Beckermann and R. Viskanta, "Mathematical modeling of transport phenomena during alloy solidification," *Appl. Mech. Rev.*, 46(1993), 1-27.
13. J. Ni and C. Beckermann, "A volume-averaged two-phase model for transport phenomena during solidification," *Metall. Trans. B*, 22B(1991), 349-361.
14. C.Y. Wang and C. Beckermann, "Equiaxed dendritic solidification with convection: I: Multiscale-Multiphase modeling," *Metall. Mater. Trans. A*, 27A(1996), 2754-2764.
15. C.Y. Wang and C. Beckermann, "Equiaxed dendritic solidification with convection: II: Numerical simulation for an Al-4 Wt Pct Cu Alloy," *Metall. Mater. Trans. A*, 27A(1996), 2765-2783.
16. C.Y. Wang and C. Beckermann, "Equiaxed dendritic solidification with convection: III: Comparisons with NH4Cl-H2O Experiments," *Metall. Mater. Trans. A*, 27A(1996), 2784-2795.
17. C. Beckermann, "Modeling segregation and grain structure development in equiaxed solidification with convection," *JOM*, 49(1997), 13-17.
18. A.V. Reddy and C. Beckermann, "Modeling of macrosegregation due to thermosolutal convection and contraction-driven flow in direct chill continous casting of an Al-Cu round ingot," *Metall. Mater. Trans. B*, 28B(1997), 479-489.
19. A. Ludwig and M. Wu, "Modeling of globular equiaxed solidification with a two-phase approach," *Metall. Mater. Trans. A*, 33A(2002), 3673-3683.
20. A. Ludwig, et al., "Simulation of Solid Movement during Solidification by a Simple Multiphase Approach," *Proc. MCWASP IX, SIM2000*, ed. P.R. Sahm et al. (Aachen: Shaker-Verlag, 2000), 175-182.
21. A. Ludwig, et al., "Numerical Description of Solid Movement during Equiaxed Solidification Using a Two-phase Modeling Approach," (Paper presented at Materials Week 2000, Munich, Germany, Sept. 25-28, 2000).
22. M. Wu, A. Ludwig, A. Bührig-Polaczek, M. Fehlbier and P.R. Sahm, "Influence of Convection and Grain Movement on Globular Equiaxed Solidification," *Intern. J. Heat Mass Transfer*, 46(2003), 2819-2832.
23. M. Wu and A. Ludwig, "Influence of Phase-Transport Phenomena on Macrosegregation and Structure Formation during Solidification," *Adv. Eng. Mater.*, 5(2003), 62-66.
24. M. Wu, A. Ludwig, P. R. Sahm and A. Bührig-Polaczek, "Grain evolution and macrosegregation in an Al-4.0%Cu casting: simulation and experimental Evalution," *Proc. MCWASP X*, ed. D.M. Stefanescu et al., (Warrendale, PA: TMS Publication, 2003), 261-268.
25. Ø. Nielsen, B. Appolaire, H. Combeau and A. Mo, "Measurements and modeling of the microstructural morphology during equiaxed solidification of Al-Cu alloys," *Metall. Mater. Trans. A*, 32A(2001), 2049-2060.
26. M. Rappaz, "Modeling of microstructure formation in solidification processes," *Intern. Mater. Rev.*, 34(1989), 93-123.
27. W. Kurz and D.J. Fisher, *Fundamentals of Solidification* (Aedemannsdorf, Switzerland: Trans Tech Publications, 1989).
28. P. Thevoz, J.L. Desbiolles and M. Rappaz, "Modeling of equiaxed microstructure formation in casting," *Metall. Trans. A*, 20A(1989), 311-322.
29. R. B. Bird, W.E.Stewart, E.N.Lightfoot, *Transport Phenomena* (New York NY: John Wiley & Sons, 1960).
30. C. Y Wang, S. Ahuja, C. Beckermann amd H.C. de Groh, "Multiparticle interfacial drag in equiaxed solidification," *Metall. Mater. Trans. B*, 26B(1995), 111-119.
31. W. Oldfield, *Trans. ASM*, 59(1966), 945-961.
32. S. V. Patankar, *Numerical heat transfer and fluid flow* (Washington DC: Hemisphere Publishing Corp., 1980).

DIRECT OBSERVATION OF PORE FORMATION AND BUBBLE MOBILITY DURING CONTROLLED MELTING AND RE-SOLIDIFICATION IN MICROGRAVITY

R. N. Grugel[1], A.V. Anilkumar[2], and C.P. Lee[3]

[1]Marshall Space Flight Center, SD46, Huntsville, AL, 35812, USA
[2]Vanderbilt University, Box 1592, Station B, Nashville, TN, 37235, USA
[3]Engineering Sciences Incorporated, Huntsville, AL, 35802

Keywords: Solidification, Porosity, GASAR, Microgravity, and Succinonitrile

Abstract

Detailed studies on the controlled melting and subsequent re-solidification of succinonitrile were conducted in the microgravity environment aboard the International Space Station (ISS) using the PFMI apparatus (Pore Formation and Mobility Investigation) located in the ISS' glovebox facility (GBX). Samples were initially prepared on ground by filling glass tubes, 1 cm ID and approximately 30 cm in length, with pure succinonitrile (SCN) under 450 millibar of nitrogen. During Space processing, experimental parameters like temperature gradient and translation speed, for melting and solidification, were remotely monitored and controlled from the ground Telescience Center (TSC) at the Marshall Space Flight Center. Real time visualization during controlled melting revealed bubbles of different sizes initiating at the solid/liquid interface, and traveling up the temperature gradient ahead of them. Subsequent controlled re-solidification of the SCN revealed the details of porosity formation and evolution. A preliminary analysis of the melt back and re-solidification and its implications to future microgravity materials processing is presented and discussed.

Introduction

The generation and inclusion of detrimental porosity, e.g., "pipes" and "rattails" can occur during controlled directional solidification processing. The origin of these defects is generally attributed to gas evolution and entrapment during solidification of the melt. On Earth, given the density difference between gas and liquid metal, an initiated bubble can rise through the liquid and exit to the atmosphere, whereas, in microgravity, the bubble is likely to get trapped in the solidified sample. Consequently, porosity inclusion diminishes the appeal of microgravity processing and therefore it is important that the nature of this problem be systematically examined, with a view to eliminating it.

The Pore Formation and Mobility Investigation (PFMI) is a systematic effort directed towards gaining an understanding of porosity formation and mobility during controlled directional solidification (DS) in the microgravity environment aboard the International Space Station (ISS). PFMI uses a pure transparent material succinonitrile (SCN), in conjunction with a translating temperature gradient stage, so that direct observation and recording of pore generation and bubble mobility can be made. PFMI examines the role of thermocapillary forces in affecting bubble dynamics, as they pertain to melting and solidification processes in a microgravity environment.